Macrospin description of the perpendicular polarizer-planar free-layer spin-torque oscillator

U. Ebels,[1] D. Houssameddine,[1] I. Firastrau,[2,3] D. Gusakova,[1] C. Thirion,[1] B. Dieny,[1] and L. D. Buda-Prejbeanu[1,4]
[1]*Spintec, CEA, CNRS, UJF, INPG; CEA/INAC, 17 Rue des Martyrs, 38054 Grenoble, France*
[2]*CEA-LETI, MINATEC, DRT/LETI/DIHS, 17 Rue des Martyrs, 38054 Grenoble, France*
[3]*Transilvania University of Brasov, 29 Boulevard Eroilor, R-500036 Brasov, Romania*
[4]*Institute Polytechnique de Grenoble, 46, Avenue Félix Viallet, 38031 Grenoble, France*
(Received 30 November 2007; published 28 July 2008)

For the "perpendicular polarizer-planar free layer" spin torque oscillator a complete current-field state diagram in the macrospin description is presented. This diagram is quite different from one of the more commonly known "planar polarizer-planar free layer" spin torque oscillators. In particular, various regions of bistability between two static states or a static and a dynamic state are evidenced in the current-field plane. The boundaries of the regions, where the static states become unstable, were deduced using a generalized ferromagnetic resonance formalism that requires only the knowledge of the second derivatives of the system energy for an arbitrary spin-polarization direction and field orientation. The dependence of the frequency as a function of current and bias field are described for the spin current induced steady-state oscillations as well as for the small amplitude damped oscillations around the static states. Finally, the results will be compared to recent experiments and the effect of temperature will be discussed.

DOI: 10.1103/PhysRevB.78.024436 PACS number(s): 72.25.Ba, 75.75.+a, 75.40.Gb, 85.70.Kh

I. INTRODUCTION

Recently it has been shown by numerous theoretical[1–13] and experimental[13–34] studies that the interaction between a spin polarized current and the local magnetization can be used to control the magnetization state of a magnetic nanostructure. In particular, it is possible to induce magnetization states that cannot be stabilized in the "conventional" way by using external static or dynamic magnetic fields. These magnetization states can be either static equilibrium states that are not energy minima or dynamic steady-state oscillations (auto-oscillations) at large precession angles. The latter allow one to explore the nonlinear regime of the magnetization dynamics whose potential exploitation for rf devices[3,20,27–31] is currently driving many research efforts. In the past, most studies have been performed for a planar spin valve[13–16,20–25,28–31] or tunnel junction structure,[17–19,32,33] where planar means that the free layer and the polarization layer are in-plane magnetized. This structure has been submitted to either in-plane bias fields[20,23,24] or very strong out-of-plane fields.[21–23]

In a recent experiment,[27] a different configuration has been explored using an out-of-plane magnetized polarizer (Pol), combined with an in-plane magnetized free layer (FL) [see Fig. 1(a)]. For this configuration large angle steady-state out-of-plane (OPP) precessions of the free layer magnetization have been obtained at the threshold current and in zero effective external field. So far not many detailed theoretical studies have been performed for this geometry,[1,35–40] which will be of potential interest for applications. We will therefore discuss here the current-field state diagram as well as the associated dynamic excitations in a zero-temperature macrospin approximation for an applied bias field H_b that is in-plane and parallel to the easy axis (see Fig. 1).

The paper is structured as follows: In Sec. II, we first present a formalism that can be considered as the extension of commonly known ferromagnetic resonance (FMR) theory including the spin torque term, which uses the second derivatives of the system energy to deduce the complex frequency. From this complex frequency the stability range of the static equilibrium state can be determined in the current-field plane for an arbitrary polarizer orientation and applied field orientation. In Sec. III we use this formalism for the "perpendicular polarizer-planar free layer" spin torque oscillator to describe its current-field state diagram and to derive expressions for the critical boundaries. In Sec. IV we address the properties of the OPP steady-state oscillations. In Sec. V we compare the macrospin simulations to recent experiments[27] to point out the role thermal activation for the experimentally determined lower critical boundary. In Sec. VI small amplitude damped oscillations around the static states will be described.

II. GENERALIZED FMR FORMALISM

As has been shown in previous publications for specific geometries,[1,5,8–13,16,37,41–44] the critical boundaries J_c vs H_b for the spin current induced static and dynamic states can be obtained by linearization of the Landau-Lifschitz-Gilbert (LLG) equation (including a spin torque term) and subsequently analyzing the stability of its solutions. This concept is well known from FMR theories.[45–47] In particular, for an arbitrary field orientation the static equilibrium position of

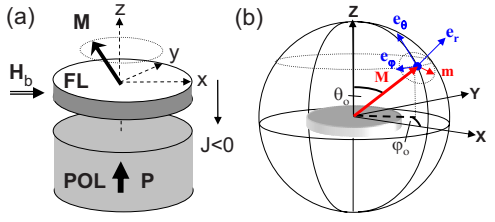

FIG. 1. (Color online) (a) Schematics of a spin torque oscillator with a perpendicularly magnetized polarizer (Pol) **P** and an in-plane magnetized free layer FL. (b) Cartesian coordinate system (X,Y,Z) and the local spherical coordinate system $(\mathbf{e}_r,\mathbf{e}_\theta,\mathbf{e}_\varphi)$(around a given static position (θ_o,φ_o).

the magnetization vector **M** is in a general case not parallel to a symmetry axis. The linearization is therefore carried out in the local spherical coordinate system $(\mathbf{e}_r, \mathbf{e}_\theta, \mathbf{e}_\varphi)$ [see Fig. 1(b)] defined by the static equilibrium position (θ_o, φ_o). This leads to a convenient definition of the resonance frequencies ω_o [Eq. (1a)] and the associated linewidth $\Delta\omega$ [Eq. (1b)] in terms of the second derivatives of the system energy $E_{\theta\theta}$, $E_{\varphi\varphi}$, and $E_{\theta\varphi}$ with respect to θ and φ:[46,47]

$$\left(\frac{\omega_o}{\gamma}\right)^2 = \frac{E_{\theta\theta}E_{\varphi\varphi} - E_{\theta\varphi}^2}{M_s^2 \sin^2\theta}, \tag{1a}$$

$$\frac{\Delta\omega}{\gamma} = \alpha\left(\frac{E_{\theta\theta}}{M_s} + \frac{E_{\varphi\varphi}}{M_s^2 \sin^2\theta}\right). \tag{1b}$$

Here γ is the gyromagnetic ratio, α is the damping constant, and M_s is the saturation magnetization. Equation (1) is evaluated at the static equilibrium positions (θ_o, φ_o) that are obtained from the zero of the first derivatives of the energy with respect to (θ, φ).

The same linearization procedure and stability analysis in local spherical coordinates is applied here for the LLG equation, including the Slonczewski[1] spin torque term that represents the interaction between a spin polarized current and the local magnetization. The corresponding equation is called LLGS [Eq. (2)]:

$$\frac{d\mathbf{M}}{dt} = -\gamma(\mathbf{M}\times\mathbf{H}_{\text{eff}}) + \frac{\alpha}{M_s}\left(\mathbf{M}\times\frac{d\mathbf{M}}{dt}\right) + \gamma\frac{a_j}{M_s}\mathbf{M}\times(\mathbf{M}\times\mathbf{P}),$$

$$\text{with} \quad a_j = \frac{\hbar}{2e}\frac{g(\eta,\theta_p)}{M_s t}J. \tag{2}$$

Here $\mathbf{H}_{\text{eff}}$ is the derivative of the system energy E with respect to **M**, which is the free layer magnetization, and **P** is the spin-polarization vector, which is parallel to the polarizer magnetization (see Fig. 1). a_j is the spin torque prefactor, which is proportional to the current density J and the spin-polarization efficiency $g(\eta, \theta_P)$ (Ref. 1), with θ_P as the angle between the polarization vector **P** and the free layer magnetization vector **M**, and η is the spin polarization.

Expressing all vectors in the local coordinate system (indicated by a prime, see Appendix A), we can write the magnetization vector $\mathbf{M}'$ and the effective field $\mathbf{H}'_{\text{eff}}$ in terms of a static and a small amplitude dynamic contribution (see Appendix B), with

$$\mathbf{M}' = \mathbf{M}'_o + \delta\mathbf{m}' = \begin{pmatrix} M_r \\ 0 \\ 0 \end{pmatrix} + \begin{pmatrix} 0 \\ \delta m_\theta \\ \delta m_\varphi \end{pmatrix} \tag{3a}$$

for the magnetization and

$$\mathbf{H}'_{\text{eff}} = \mathbf{H}'_{\text{eff}}(\mathbf{M}'_o)\big|_{\text{static}} + \mathbf{h}'_{\text{eff}}\big|_{\text{dynamic}} \tag{3b}$$

for the effective field.

Inserting Eq. (3) into the LLGS Eq. (2), neglecting terms of second order in the dynamic contributions $\delta\mathbf{m}'$ and h'_{eff}, and solving for solutions of the form δm_θ, $\delta m_\varphi \sim e^{-i\omega t}$, leads to the generalized complex frequency, $\omega = \omega' + i\omega''$ [Eq. (4)], with ω' as the real part and ω'' as the imaginary part, and

$$\frac{\omega}{\gamma'} = -\frac{i}{2}\left(\frac{\Delta\omega}{\gamma} - 2a_j P'_r\right)\Bigg|_{\theta_o,\varphi_o} \pm \sqrt{-\frac{1}{4}\left(\frac{\Delta\omega}{\gamma} - 2a_j P'_r\right)^2 + (1+\alpha^2)\left(\frac{\omega_o}{\gamma}\right)^2 + (1+\alpha^2)(a_j P'_r)^2}\Bigg|_{\theta_o,\varphi_o},$$

$$\gamma' = \frac{\gamma}{1+\alpha^2} \quad P'_r = P_x \sin\theta_o \cos\varphi_o + P_y \sin\theta_o \sin\varphi_o + P_z \cos\theta_o, \tag{4}$$

Here $P' = (P'_r, P'_\theta, P'_\varphi)$ is the polarization vector in the local spherical coordinates. All terms are evaluated at the static states (θ_o, φ_o) that are solutions of Eq. (5);

$$0 = -\gamma\mathbf{M}\times\mathbf{H}_{\text{eff}} + \gamma\frac{a_j}{M_s}[\mathbf{M}\times(\mathbf{M}\times\mathbf{P})] \tag{5a}$$

$$\Leftrightarrow \begin{cases} -\dfrac{E_\varphi}{M_s \sin\theta} - a_j P'_\theta = 0 \\ \dfrac{E_\theta}{M_s} - a_j P'_\varphi = 0 \end{cases}. \tag{5b}$$

Equation (5a) is identical to setting $d\mathbf{M}/dt$ to zero in the LLGS equation (using either coordinate system of Fig. 1), which means that the static states are defined by the equilibrium between the precession torque and the spin torque. Equation (5b) is equivalent to Eq. (5a), upon expressing H'_{eff} by the corresponding derivatives of the energy with respect to (θ, φ) (see Appendix B). This equation is useful when solving numerically for the static states, while Eq. (5a) is more useful when looking for analytic expressions. To note, the static solutions of Eq. (5) under spin torque can be in specific cases very far from an energy minimum or energy maximum,[6] which are the solutions in the absence of spin torque. This is, for example, the case for the perpendicular polarizer, as will be demonstrated in Sec. III B.

The generalized complex frequency of Eq. (4) has two terms, a "linewidth" term (first term) and a square-root term (second term), which contain the zero-current expressions ω_o and $\Delta\omega$ given by Eq. (1). Setting $a_j = 0$ in Eq. (4), one therefore recovers the frequency (square-root term) and associated linewidth (first term) known from general FMR theory.[45–47] The frequency will include small contributions

due to damping, which are neglected in most cases [as in Eq. (1a)].

In the presence of spin torque, the generalized complex frequency ω [Eq. (4)] is evaluated here to determine the stability of the solutions of Eq. (5). For this we have to analyze the imaginary part ω'' of Eq. (4) for which three different cases can be distinguished:

Case 1: If the imaginary part of Eq. (4) is negative, $\omega''<0$, perturbations decay in time, and the static state (θ_o,φ_o) is stable. If, furthermore, the square-root term in Eq. (4) is real, we obtain small amplitude damped oscillations around the considered static position whose frequency is given by the real part (square-root term) of ω and whose linewidth is given by the imaginary part of ω (first term).

Case 2: If the imaginary part is positive, $\omega''>0$, the perturbation amplitude diverges and the considered position is not a stable state.

Case 3: The zero of the imaginary part, $\omega''=0$, therefore provides the instability lines as a function of the two control parameters, current density and bias field, at which the static stable states transition into another static or dynamic state. Several cases can be distinguished depending on whether the square-root term of Eq. (4) is real or imaginary.

(3a) In case the square-root term is real, the imaginary part ω'', and with this the condition for the critical current J_c, is given by the first term (the linewidth term) in Eq. (4).

(3b) In case the square-root term is imaginary, there is no real part and the critical boundary J_c is determined by both the linewidth term and the square-root term of Eq. (4).

(3c) If the component P_r' of the polarization vector is zero, the condition for the instability boundary is given by $\omega_o=0$. As will be shown below (Sec. III B), this is the case for the boundary J_{c1} of the perpendicular polarizer.

In summary, Eq. (4) provides a convenient way to determine the complex frequency for an arbitrary orientation of the spin-polarization vector $\mathbf{P}$ and the applied bias field $\mathbf{H}_b$, by only knowing the polarization vector $\mathbf{P}'$ in the local spherical coordinates and the second derivatives of the energy evaluated at the stable points (θ_o,φ_o). From this one can determine (i) the critical boundaries J_c as a function of bias field H_b for which the static states become unstable (Sec. III) and (ii) the small angle damped oscillations around the stable static states (Sec. VII).

It is noted that Eq. (4) has been derived by neglecting the linearization of the angular dependent prefactor of $a_j(\theta_p)$. Furthermore, Eq. (4) can easily be rewritten in order to include a fieldlike (or exchange) term.[48] It is also noted that this formalism is applicable when the spin torque induced trajectories are not close to constant energy trajectories, which occurs when the spin polarization does not coincide with a symmetry axis. Finally, the formalism is limited to the "uniform mode" macrospin description and is thus less general than the nonlinear spin-wave theories described in Refs. 8–10 and 43.

III. STATIC STATES AND STATE DIAGRAM

In the following we will apply the above FMR formalism to the "perpendicular polarizer-planar free layer" spin torque oscillator illustrated in Fig. 1(a). The corresponding polarization vector $\mathbf{P}$ of the polarizer is given in Eq. (6a) and the energy of the free layer, described in a thin film geometry [see Fig. 1(b)], is given by Eq. (6b):

$$\mathbf{P}=(P_x,P_y,P_z)=(0,0,1), \tag{6a}$$

$$E=K_u[1-m_x^2]-\mathbf{M}\mathbf{H}_b+2\pi M_s^2 m_z^2$$

$$\text{with}\quad \mathbf{m}=\frac{\mathbf{M}}{M_x}=(m_x,m_y,m_z). \tag{6b}$$

Here K_u is a uniaxial anisotropy energy constant, taking either a magnetic anisotropy or a shape anisotropy into account. The external bias field H_b is oriented in-plane and parallel to the in-plane easy axis ($\|X$). This field orientation is motivated by the experiments where a third in-plane magnetized analyzing layer is required to monitor the magnetization motion of the free layer.[27] This analyzing layer and the free layer form a planar spin valve substructure whose magnetoresistance is studied under in-plane bias fields. It is noted though that a spin torque effect from this planar analyzer will be neglected in the theoretical description here. Its effect does not alter the major characteristics, as has been tested by additional simulations (not shown here).[49]

Furthermore, for simplicity we take the spin-polarization efficiency constant $g(\eta,\theta_P)=g(\eta)=$const, where we evaluate $g(\eta)$ for $\theta_p=90°$ from the expression first introduced by Slonczewski [see Eq. (14) of Ref. 1] $\theta_p=90°$ corresponds to the zero-current orientation between the polarizer (out-of-plane) and the free layer magnetization (in-plane).

In the following we first derive the static solutions from Eq. (5) (Sec. III A) and analyze their stability in Sec. III B, from which the current-field state diagram is deduced. Numerical evaluation is carried out using the material parameters given in Table I that are chosen with respect to the experiments.[27]

TABLE I. Parameters used for the numerical evaluation of the different equations throughout the text. Here H_u is the uniaxial anisotropy field, φ_o is the free layer saturation magnetization, α is the damping constant, η is the spin polarization, $g(\eta,\theta_p)$ is the spin-polarization efficiency, γ is the gyromagnetic ratio, t is the free layer film thickness, and A is the free layer surface area. The values were chosen with respect to the experiments described in Ref. 27.

$H_u=2K_u/M_s$	100 Oe (8 kA/m)
M_s	880 emu/cm^3 (or kA/m)
α	0.02
η	0.3
$g(\eta,\theta_p=90°)$	0.17
γ	17.6×10^6 (Oe s)$^{-1}$
t	3.5 nm
A	$0.25\pi60\times70$ nm^2

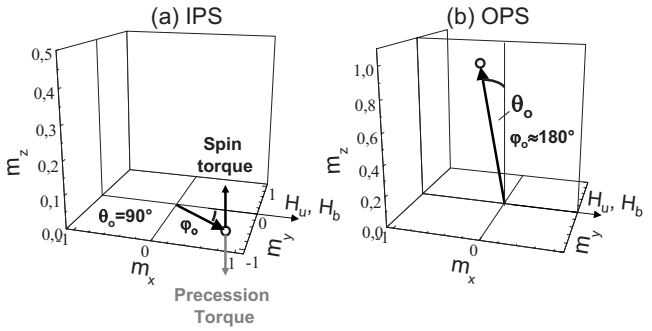

FIG. 2. Schematics showing (a) the IPS state (for $J<0$) and the equilibrium of the spin torque (upward arrow) and the precession torque (downward arrow); (b) the OPS state.

A. Static solutions

In order to determine the static solutions, we solve Eq. (5a) in Cartesian coordinates, which is more convenient for the perpendicular polarizer geometry. This leads to the following equations for the three torque components τ_x, τ_y, and τ_z [Eq. (7)]:

$$\tau_x = H_d m_y m_z + a_j m_x m_z = 0, \tag{7a}$$

$$\tau_y = -H_d m_y m_z - (H_u m_x + H_b) m_z + a_j m_y m_z = 0, \tag{7b}$$

$$\tau_z = (H_u m_x + H_b) m_y - a_j (1 - m_z^2) = 0. \tag{7c}$$

Here we define the demagnetization field as $H_d = 4\pi M_s$ and the uniaxial anisotropy field as $H_u = 2K_u / M_s$.

In-plane stable state (IPS). Inspection of Eq. (7) leads to a first solution [Eq. (8)] given by

$$m_z = 0 \quad \text{and} \quad H_u m_x m_y + H_b m_y = a_j, \tag{8}$$

equivalent to

$$\theta_o = 90° \quad \text{and} \quad H_u \sin\varphi_o \cos\varphi_o + H_b \sin\varphi_o = a_j.$$

For $a_j = 0$, we see that this corresponds to the in-plane energy minima at $\varphi = 0°$ or $\varphi = 180°$, while for $a_j \neq 0$ this corresponds to an in-plane rotation φ_o (at $\theta_o = 90°$) away from the energy minima as illustrated in Fig. 2(a). This new position is therefore called in-plane stable (IPS) state. Here φ_o can be relatively large, as will be evaluated further below. The in-plane rotation by φ_o means that the spin torque is pushing the magnetization uphill on the energy surface until the spin torque is balanced by the precession torque [Eq. (7c)], which has an out-of-plane component only for $\varphi_o \neq (0°, 180°)$. Depending on the current direction, the in-plane rotation φ_o is either clockwise ($J<0$) or counterclockwise ($J>0$).

Out-of-plane stable state (OPS). A second solution of Eq. (7) is given by Eq. (9a):

$$\text{if } a_j \neq 0: \quad m_x = -\frac{H_b}{H_d + H_u + \dfrac{a_j^2}{H_d}}, \quad m_y = -\frac{a_j}{H_d} m_x,$$

$$m_z = \pm\sqrt{1 - m_x^2 - m_y^2}, \tag{9a}$$

$$\text{if } a_j = 0: \quad \varphi_o = 180° \quad \text{and} \quad m_x = \sin\theta_o = -\frac{H_b}{H_u + H_d}. \tag{9b}$$

This solution (see Appendix C) derives from the out-of-plane energy maximum [Eq. (9b)] at zero current ($a_j = 0$), which is characterized by a large m_z and small m_x component. This solution is therefore called out-of-plane stable (OPS) state [see Fig. 2(b)]. A similar state has been examined in Ref. 8 for the planar polarizer.

In our sign convention of the spin transfer torque term Eq. (2), the free layer magnetization in the OPS state is antiparallel to the spin-polarization vector **P** for positive current ($m_z < 0$) and parallel for negative current ($m_z > 0$).

To note, the effect of the a_j^2 / H_d term in Eq. (9a) is a small rotation of the magnetization out of the x-z plane, which can be neglected in most situations of interest ($a_j < 0.1 H_d$). In this case the OPS state can be well approximated by Eq. (9b).

B. Stability, critical lines, and state diagram

Inserting the static solutions IPS [Eq. (8)] and OPS [Eq. (9)], which depend on the current density and bias field, into the generalized complex frequency [Eq. (4)], the stability range of these solutions is determined from the condition of the zero of the imaginary part, $\omega'' = 0$. This provides the critical currents J_{c1} and J_{c2} for the IPS and OPS states, respectively. From the discussion of the corresponding state diagram and from comparison to numerical integration of LLGS [Eq. (2)], various bistable regions become evident that introduce two further critical currents J_{c3} (Ref. 40) and J_{c4}. With this, the range of steady-state precession depends sensitively on whether the current is increased from zero or decreased from a sufficiently large value. In the following we first discuss the stability range for the IPS state for increasing current.

1. Stability range of the IPS state

The solution of $\omega'' = 0$ of Eq. (4) for the IPS state corresponds to case (3c) (Sec. II), since with $\theta_o = 90°$ the P_r' term is zero. This is equivalent to $\omega_o = 0$ or $E_{\varphi\varphi} = 0$, leading to a condition for a maximum (critical) in-plane rotation angle φ_c [Eq. (10a)] and its associated critical current density J_{c1} [Eq. (10b)]:

$$\cos\varphi_c = -\frac{H_b}{2H_u} \pm \sqrt{\left(\frac{H_b}{2H_u}\right)^2 + 0.5}, \tag{10a}$$

$$J_{c1} = \frac{2e}{\hbar}\frac{M_s t}{g(\eta)} \times (H_u \sin\varphi_c \cos\varphi_c + H_b \sin\varphi_c). \tag{10b}$$

Equation (10a) gives four solutions for φ_c. The positive and negative roots correspond to initial zero-current magnetization states oriented either along 0° or 180°, respectively. This is combined with a positive and negative sign of φ_c, corresponding to negative and positive current, respectively.

Before discussing the four branches of the critical current density J_{c1} and the resulting state diagram shown in Fig.

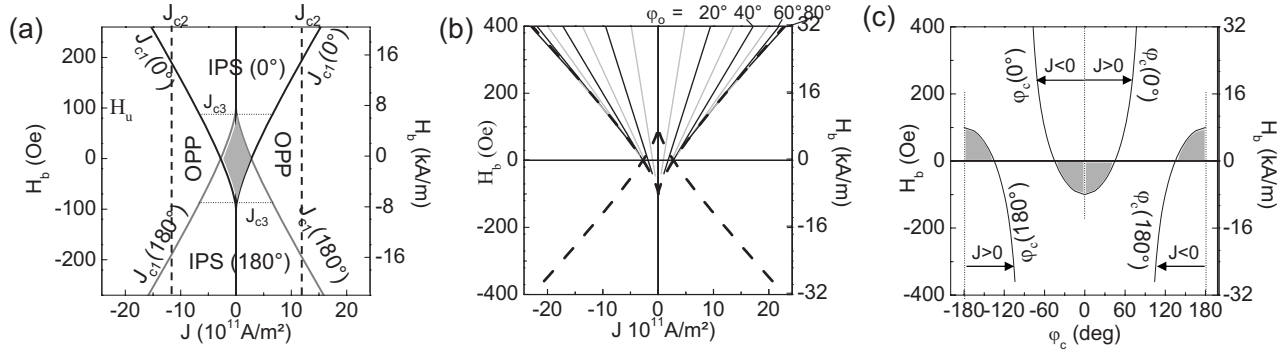

FIG. 3. (a) State diagram with critical lines J_{c1} (0°) and J_{c1} (180°). IPS 0° and IPS 180° are the in-plane static states corresponding to an initial (zero current) magnetization orientation of φ=0° or 180°. OPP indicates the region of out-of-plane precession. The gray diamond shaped region around zero-current and zero-bias field is the bistable static region IPS 0°/IPS 180°. The vertical dashed bold lines indicate J_{c2}. The horizontal dotted thin lines indicate the boundary J_{c3}, which is obtained only from numerical integration of LLGS and which depends on the rise time used to apply the current (see Ref. 40). (b) Lines of constant equilibrium angle φ_o in the field-current plane. Black lines $\varphi_o = \pm 20°, 40°, 60°, 80°$; gray dashed lines $\varphi_o = \pm 10°, 30°, 50°, 70°$; (c) Critical in-plane angle φ_c as a function of bias field according to Eq. (10). The arrows indicate that the magnetization rotates either from φ_o=0° to φ_c (0°) or from φ_o=180° to φ_c (180°). The gray shaded areas correspond to the case when the magnetization and the applied bias field are antiparallel, as in (a).

3(a), we want to give an interpretation for the condition of the critical angle φ_c. Let us remember that the IPS static state represents a balance between the spin torque and the precession torque [Eq. (7c)]. The latter has only contributions from the anisotropy field and the bias field. It therefore has a maximum between the in-plane easy axis (φ=0°,180°) and the in-plane hard axis ($\cos\varphi = -H_b/H_u$ for $|H_b| < H_u$ and $\cos\varphi = -1$ for $|H_b| > H_u$). Consequently the spin torque is balanced by the precession torque only for as long as the in-plane rotation angle φ_o is smaller than a critical angle φ_c corresponding to the maximum of the precession torque. Setting, therefore, the derivative (with respect to φ) of the z component of the precession torque τ_z^{Pr} to zero [equal to Eq. (7c) with a_j=0], we obtain the same solution for φ_c;

$$\frac{d\tau_z^{\mathrm{Pr}}}{d\varphi} = \frac{d}{d\varphi}(H_u \sin\varphi \cos\varphi + H_b \sin\varphi) = 0 \Leftrightarrow \text{Eq. (10a)}.$$

The four branches of the critical current density J_{c1} are plotted in Fig. 3(a) and are denoted $J_{c1}(0°)$ and $J_{c1}(180°)$, according to whether the initial (zero current) state is along 0° [positive root of Eq. (10a)] or 180° [negative root of Eq. (10a)].

These critical lines mean that, upon increasing the amplitude of the current density from zero up to $|J| \le |J_{c1}|$, the static states IPS 0° and IPS 180° are stable with a corresponding in-plane rotation angle φ_o away from the initial state that is smaller or equal to the critical angle φ_c. At φ_c this static state becomes unstable.

From numerical integration of the LLGS equation [Eq. (2)], it is obtained that for $|J| > |J_{c1}|$ the magnetization goes into steady-state out-of-plane precessions (OPPs),[35] which are illustrated in Fig. 4. This transition from the IPS to the OPP state is accompanied by an abrupt jump of the out-of-plane magnetization component from m_z=0 (θ=90°) to $|m_z| > 0$ (θ<90° for J<0 and θ>270° for J>0). Although the steady-state out-of-plane oscillations will be discussed in detail in Sec. IV, we will give here a brief definition. For the energy surface considered [Eq. (6b)], the OPP oscillations correspond to large angle precessions of the magnetization around the out-of-plane energy maximum[8] [Eq. (9)]. They are stabilized because the spin torque that pushes the magnetization out-of-plane balances in average the damping torque, which pulls the magnetization in-plane.[27,35] If the free layer is associated with a third in-plane magnetized reference (or analyzing) layer, as in a spin valve or magnetic tunnel junction, this precessional motion of the free layer magnetization on OPP trajectories gives rise to large magnetoresistance variations. This is in contrast to the in-plane precession (IPP),[20,23,24] induced by a planar polarizer system where the overall in-plane projection is smaller. Stabilizing steady-state OPP oscillations will therefore be of great interest for applications in rf components.

Coming back to the IPS state, it is noted that the in-plane rotation angle φ_o is not small, as is illustrated in Fig. 3(b), where the lines of constant φ_o are plotted in the current-field plane (for an initial state along 0°). Two cases need to be distinguished, for which the initial magnetization and the applied bias field are either (i) parallel or (ii) antiparallel. We consider first the more important parallel case (i). Here φ_o

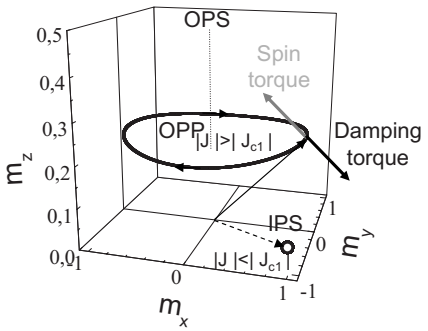

FIG. 4. Stable IPS state (open point) for $|J| < |J_{c1}|$ and steady-state OPP oscillations (full line) for $|J| < |J_{c1}|$. The arrows indicate the balance between the damping torque (black) and the spin torque (gray).

increases with increasing current amplitude up to the critical angle φ_c but decreases with increasing field amplitude. These dependencies are a direct consequence of the balance between the precession torque (decreasing φ_o) and the spin torque (increasing φ_o) [Eq. (7c)].

In addition, for increasing bias field amplitude, the in-plane hard axis is shifted away from the $\varphi=90°$ orientation ($\cos\varphi=-H_b/H_u$ for $|H_b|<H_u$ and $\cos\varphi=-1$ for $|H_b|>H_u$). Consequently, for increasing values of H_b, the critical angle φ_c at which the IPS state becomes unstable increases (for an initial state along 0°) from $\varphi_c=45°$ at $H_b=0$ to $\varphi_c=90°$ at $H_b>H_u$ [see Fig. 3(c)]. A larger current-density amplitude is thus required for the transition from IPS to OPP. This explains qualitatively the almost linear increase in the absolute value of the critical current density J_{c1} with increasing bias field amplitude, for both positive and negative fields and both positive and negative currents [see Fig. 3(a)].

For the second case (ii), where the magnetization and the applied bias field are antiparallel, the arguments are reversed. Here φ_o increases with increasing bias field amplitude (for an initial state along 0°), thus lowering the critical current amplitude with increasing $|H_b|$ and going to zero when $|H_b|=H_u$. For $|H_b|>H_u$ the magnetization reverses and the magnetization is again parallel to the bias field.

The four branches of J_{c1} therefore define a bistable region for $|H_b|\leq H_u$ [gray region in Fig. 3(a)] where both the IPS 0° and IPS 180° states are stable.[40] In this field range, $|H_b|\leq H_u$, two critical current lines exist when increasing the current amplitude from zero. The critical line with lower value corresponds to the case when the bias field and initial magnetization state are antiparallel and the critical line with larger amplitude corresponds to the case when the bias field and the initial magnetization are parallel.

An important consequence of this bistable region is that in magnetoresistance curves vs bias field the coercive field should decrease with increasing current amplitude for as long as the current amplitude is smaller than the zero-field critical current, $|J|<|J_{c1}|(H_b=0)$.

Another less important consequence is that, starting with an antiparallel configuration, there is a small bistable region IPS/OPP bounded by $J_{c1}(180°)$, $J_{c1}(0°)$, and a third critical boundary that we have introduced as J_{c3} in a previous publication.[40] This boundary is indicated in Fig. 3(a) by a horizontal dotted line at $|H_b|\approx H_u$. It is, however, of less importance and will not be considered here.

2. Stability range of the OPS state

The stability range of the OPS state is obtained by inserting the approximate OPS equilibrium condition Eq. (9b) into Eq. (4). Since the square-root term is real, the condition of $\omega''=0$ is equivalent to setting the linewidth term of Eq. (4) to zero [case (3a) of Sec. II], yielding the critical current density J_{c2} as given by Eq. (11a):

$$-\frac{i}{2}\left(\frac{\Delta\omega}{\gamma}-2a_jP_r'\right)=0$$

$$\Leftrightarrow$$

$$J_{c2}=\frac{2e}{\hbar}\frac{M_st}{g(\eta)}\cdot\frac{\alpha}{2}\left[\frac{H_b^2-(H_u+H_d)(H_u+2H_d)}{\sqrt{(H_u+H_d)^2-H_b^2}}\right], \tag{11a}$$

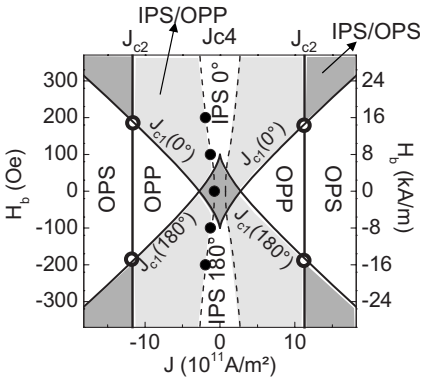

FIG. 5. State diagram showing the three critical currents J_{c1} (0°,180°) (thin full line), J_{c2} (vertical thick full line), and J_{c4} (dashed line and dots). The dots were obtained from numerical integration of LLGS and the dashed line from a quasianalytical evaluation, Sec. IV B. The bistable IPS/OPP regions are indicated by light gray areas, while the bistable IPS/OPS regions are indicated by dark gray areas.

$$J_{c2}\approx\left[\frac{2e}{\hbar}\frac{M_st}{g(\eta)}\right]\cdot\alpha\left(H_d+\frac{H_u}{2}\right). \tag{11b}$$

Since H_b remains small with respect to H_d (for practical cases of interest), the critical boundary J_{c2} can be well approximated by Eq. (11b) which is independent of H_b.

This critical boundary J_{c2} is shown in Fig. 3(a) by the two vertical dashed lines and is discussed in more detail in the next paragraph in context of Fig. 5, which shows the complete diagram and the different regions of bistability.

C. State diagram and bistability

The two critical lines J_{c1} and J_{c2} intersect at some field value (see open circles in Fig. 5) so that, only for low bias fields, we have $|J_{c1}|>|J_{c2}|$, while for large bias fields we have $|J_{c1}|>|J_{c2}|$. Consequently for low bias fields one traverses the following sequence of states upon *increasing the current-density amplitude* from zero: IPS→OPP→OPS. The steady-state OPP oscillations therefore seem to exist only in a triangular shaped region bounded by $J_{c1}(0°)$, $J_{c1}(180°)$, and J_{c2}.

In contrast to this, in the field range where $|J_{c1}|>|J_{c2}|$, steady-state OPP oscillations do not exist for increasing current-density amplitude. Here the system starts with an IPS state at low current density and stays in an IPS state upon crossing J_{c2}. It then goes directly into OPS upon crossing J_{c1}. The reason for this is that upon increasing the current-density amplitude the spin torque has to rotate the magnetization first up to the critical angle φ_c [see Eq. (10)] before the IPS state becomes unstable and the magnetization transitions into another state. However, at J_{c1} the current density is so strong that the corresponding out-of-plane magnetization component is so large that immediately an OPS state is obtained. We come back to this in Sec. IV B (Fig. 6) where the out-of-plane magnetization component of the OPP oscillation is discussed in more detail.

Upon reducing the current-density amplitude from this OPS state back into the region $|J_{c2}|<|J|<|J_{c1}|$, the magneti-

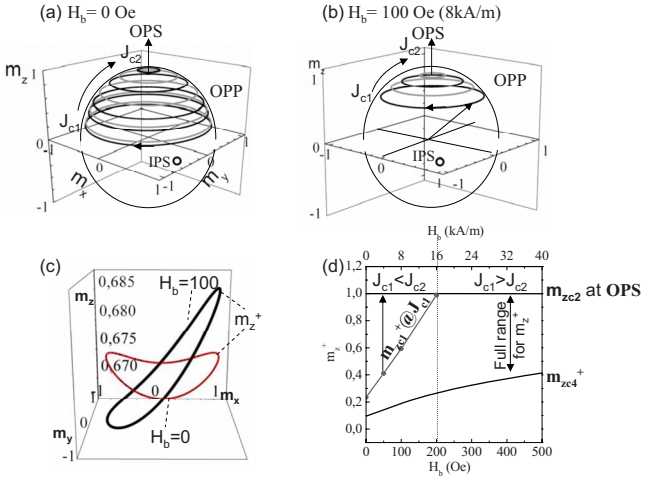

FIG. 6. (Color online) (a) $H_b=0$ OPP trajectories. The open dot represents the IPS state for $|J|<|J_{c1}|$ (for $J<0$). Black and gray lines are for $|J|>|J_{c1}|$ with $J_{c1}=-0.925\times10^{11}/\mathrm{m}^2$ and $J=-0.927$, -1.11, -1.67, -1.85, -2.22, -2.78, -3.33, -3.7, and -4.1×10^{11} $\mathrm{A/m}^2$. (b) $H_b=100$ Oe (8 kA/m) OPP trajectories for $|J|>|J_{c1}|$ with $J_{c1}=-2.4\times10^{11}$ $\mathrm{A/m}^2$ and $J=-2.78$, -3.33, -3.7, and -4.1×10^{11} $\mathrm{A/m}^2$. (c) Comparison of $H_b=0$ and $H_b=100$ Oe (8 kA/m) trajectories for $J=-2.8\times10^{11}$ $\mathrm{A/m}^2$. For $H_b=0$ the spin current induced trajectories (red points) are close to constant energy trajectories (black points) and are therefore difficult to distinguish. The definition of the m_z^+ component at $\varphi=0°$ is indicated on the trajectory. (d) Calculated range of m_z^+ ranging between the saddle point trajectory m_{zc1}^+ and the OPS state m_{zc2}. The m_{zc1}^+ values at the critical boundary J_{c1} are shown by the gray line with $m_{zc4}^+<m_{z1}^+<m_{zc2}$.

zation now remains in the OPS state. This defines the four bistable regions that are shown by the dark gray areas in Fig. 5 labeled IPS/OPS.

The remaining question is, what happens when the current-density amplitude is further reduced from the bistable IPS/OPS region ($|J_{c2}|<|J|<|J_{c1}|$) to below $|J_{c2}|$? Since the critical current density J_{c2} is derived from condition (3a) (Sec. II) of the complex frequency with a nonzero real part ω' [square-root term of Eq. (4)], one would conclude that upon decreasing the current-density amplitude to below J_{c2}, the OPS state gives way to a precession state. This is confirmed from numerical integration of LLGS, which reveals that starting from the OPS state and upon reducing the current-density amplitude to below $|J_{c2}|$ (for both regions $|J_{c1}|<|J|<|J_{c2}|$ and $|J_{c2}|<|J|<|J_{c1}|$) the system goes into steady-state OPP oscillations.

These steady-state OPP oscillations are maintained when decreasing the current-density amplitude down to a critical boundary that is shown as J_{c4} in Fig. 5 (dashed line and dots). J_{c4} is calculated in Sec. IV B using the fact that the OPP trajectories are close to constant energy trajectories.

In summary, the zero-temperature macrospin state diagram for the "perpendicular polarizer-planar free layer" oscillator contains only three regions where only one state is stable (white areas in Fig. 5), independent of the field and current history. These are (i) the IPS state for $-J_{c4}<J<J_{c4}$, (ii) the OPP state when $|J_{c1}|<|J|<|J_{c2}|$, and (iii) the OPS state for $J>|J_{c2}|>|J_{c1}|$ or $J>|J_{c1}|>|J_{c2}|$. The other parts of the diagram (light and dark gray areas in Fig. 5) are bistable regions between the IPS and OPP or IPS and OPS states and depend on the history of applied current and field.

An important consequence of the bistability is that the current and field ranges where OPP oscillations can be excited are more enlarged, extending from J_{c4} to J_{c2} (light gray areas in Fig. 5). In particular, for the case of large uniaxial anisotropy values for which in the whole field range $|J_{c1}|>|J_{c2}|$ ($\Leftrightarrow 0.5H_u>\alpha H_d$), it will still be possible to induce OPP oscillations when reducing the current amplitude from above $|J_{c1}|$.

Finally, we note that, in the whole field range $|H_b|\leq H_d$, the lower critical boundary J_{c4} does not cross J_{c1} or J_{c2}: $|J_{c4}|<|J_{c1}|$ and $|J_{c4}|<|J_{c2}|$.

IV. OPP STEADY-STATE OSCILLATIONS FOR $|J_{c4}|<|J|<|J_{c2}|$

With respect to the experiments, one of the most important parameters is the precession frequency of the spin polarized current induced steady-state OPP oscillations and its dependence on current density and bias field. For this, one first has to take a closer look at the OPP trajectories.

A. Steady-state OPP trajectories

In Figs. 6(a) and 6(b) the trajectories of steady-state OPP oscillations are plotted for current-density amplitudes that are between $|J_{c1}|$ and $|J_{c2}|$. They have been obtained by numerical integration of LLGS [Eq. (2)]. These trajectories are relatively flat, see Fig. 6(c), with little variation of the m_z component along the trajectory. In addition, for $H_b=0$, they are symmetric with respect to $m_x=0$ while they are asymmetric and tilted for $H_b\neq0$ [see Fig. 6(c)].

Using the fact that the OPP trajectories are relatively flat and that they are stabilized due to the balance between the spin torque and the damping torque (see Fig. 4), one can derive an approximate expression for the averaged m_z component $\langle m_z\rangle$ in the limit that H_b is zero.[35] For the perpendicular polarizer the spin torque has only a θ component. Therefore, upon setting the average over one precession period of the θ component of the sum of the damping torque $\tau_\theta^{\mathrm{Gb}}$ and the spin torque $\tau_\theta^{\mathrm{ST}}$ to zero [Eq. (12a)], we obtain $\langle m_z\rangle$ [Eq. (12b)]:[35]

$$\langle\tau_\theta\rangle=\langle\tau_\theta^{\mathrm{ST}}+\tau_\theta^{\mathrm{Gb}}\rangle=0,$$

$$\tau_\theta^{\mathrm{ST}}=\gamma' a_j M_s\sin\theta,$$

$$\tau_\theta^{\mathrm{Gb}}=-\alpha\gamma' M_s(-0.5H_u\sin2\theta\cos^2\varphi-H_b-0.5H_d\sin2\theta), \tag{12a}$$

$$\langle m_z\rangle=\cos\theta=-\frac{a_j}{\alpha(H_d+0.5H_u)}\approx\frac{a_j}{\alpha H_d}. \tag{12b}$$

From Eq. (12b) one can see that the damping torque is dominated by the demagnetization field torque, supposing small values of the uniaxial anisotropy, as is the case in most experiments. Furthermore, from Eq. (12b) it is evident that

$\langle m_z \rangle$ of the steady-state OPP oscillations increases with increasing current amplitude [as shown in Figs. 6(a) and 6(b)]. In other words, for increasing spin torque amplitude the magnetization is pushed onto trajectories of higher and higher energy. At the same time the diameter of the trajectories decreases and converges to the OPS stable state. Thus, by setting $\cos\theta \approx 1$, we retain the expression for the critical current J_{c2} given in Eq. (11b).

B. Constant energy trajectories and lower critical boundary J_{c4}

The torque due to the spin polarized current is generally of the order of the damping torque and both are small with respect to the precession torque.[6–11,41–43] As a consequence, in most situations of interest, the trajectories of spin current induced steady-state oscillations can be well approximated by constant energy trajectories for which $\alpha=0$ and $J=0$ so that they are described only by the conservative precession term [first term of Eq. (2)]. Although this is not correct for an arbitrary spin-polarization direction, this is a good approximation for the steady-state OPP trajectories induced by a perpendicularly polarized spin current. This is demonstrated in Fig. 6(c) in the case of $H_b=0$ where the constant energy trajectory (black dots) is superposed onto the spin current induced trajectory (red dots). From this approximation we calculate a number of properties, as will be discussed in the following:

To characterize an OPP trajectory, we use the maximum value of the m_z component on the trajectory at $\varphi=0°$ indicated in Fig. 6(c) by m_z^+. The range of possible m_z^+ values can be calculated directly from the initial energy $E_o=E(\varphi_o=0°, \cos\theta_o=m_z^+)$ using Eq. (6b) and keeping in mind that the energy of OPP constant energy trajectories has an upper and a lower bound.[8–11,41,42] The upper bound is given by the energy maximum and thus by the OPS state [Eq. (9), Sec. III A]. The corresponding m_z component is therefore called m_{zc2}. The lower bound is given by the energy of the saddle point that corresponds to the in-plane hard axis. The corresponding component is called m_{zc4}^+.

In Fig. 6(d), this range of m_z^+ values $[m_{zc4}^+, m_{zc2}]$ is shown as a function of the bias field H_b (for the case of negative current density). While m_{zc2} is more or less constant, m_{zc4}^+ increases with H_b. Superposed onto this graph are the m_z^+ values at the critical current density J_{c1} called m_{zc1}^+, as calculated from numerical integration of LLGS. As can be seen, m_{zc1}^+ is much larger than m_{zc4}^+. This means that upon increasing the spin current amplitude from zero to the critical current density $|J_{c1}|$, the system does not jump into its lowest-energy OPP trajectory. However, due to the bistable IPS/OPP region described in Sec. III C (Fig. 5), the low-energy OPP trajectories are accessible when the current density is reduced from an OPP state at $|J| \geq |J_{c1}|$ to a value $|J_{c4}| < |J| < |J_{c1}|$. From this it is evident that the lower boundary J_{c4} of Fig. 5 is given by the saddle point trajectory defined by m_{zc4}^+.

We have calculated J_{c4} approximately by using the fact that for a periodic oscillation, the integral of the energy loss along one precession period has to be zero [Eq. (13a)]:[11,41,42]

$$\oint \frac{dE}{dt} dt = 0. \tag{13a}$$

From this it follows for the boundary J_{c4}:

$$J_{c4} = \frac{2e}{\hbar} \frac{M_s t}{g(\eta)} \frac{\alpha \oint (\mathbf{M} \times \mathbf{H}_{\text{eff}})^2 dt}{\oint (\mathbf{M} \times \mathbf{H}_{\text{eff}})(\mathbf{M} \times \mathbf{P}) dt - \alpha M_s \oint \mathbf{P}(\mathbf{M} \times \mathbf{H}_{\text{eff}}) dt}$$

$$= \frac{2e}{\hbar} \frac{M_s t}{g(\eta)} \alpha \times \text{Int}_{c4} \quad dt = \frac{dm_x}{\dot{m}_x}; \quad \dot{m}_x = \gamma H_d m_z m_y; \tag{13b}$$

Here the integration is along a constant energy trajectory that passes close to the saddle point. It is parametrized in terms of the m_x component upon expressing m_y and m_z as a function of m_x using the constant norm $|\mathbf{m}|=1$ and upon replacing the time integration as given in Eq. (13b). The numerical evaluation of Eq. (13b) for J_{c4} is plotted in Fig. 5 (dotted line) and is compared with the numerical integration of the LLGS [Eq. (2)] (dots). Both approaches show good agreement. A detailed discussion of J_{c4} and its dependence on α, H_u, and M_s will be presented in Sec. IV D.

C. OPP precession frequencies

Using the same approximation of constant energy trajectories, one can also deduce the precession frequency as a function of current and bias field. For this we evaluate the time integral or inverse frequency for a given constant energy trajectory characterized by m_z^+. This yields $f(m_z^+)$ [Eq. (14)]:

$$f^{-1} = T = \oint dt = \oint \frac{dm_x}{\dot{m}_x}. \tag{14}$$

We then determine the required current density $J(m_z^+)$ using Eq. (13) in its more general form for an arbitrary conservative trajectory characterized by a given m_z^+. The relation between m_z^+ and J for the full range of steady-state OPP oscillations ($|J_{c4}| < |J| < |J_{c2}|$) is shown in Fig. 7(a) for different bias field values H_b. m_z^+ is a measure of the precession amplitude for OPP oscillations. At large current densities, the m_z^+ values converge to the OPS state.

Combining $J(m_z^+)$ and $f(m_z^+)$, one then obtains the frequency vs J. The results of the numerical evaluation are shown in Figs. 7(b) and 7(c) (full lines) and are compared to the solutions derived by numerical integration of LLGS (points), which reveal good agreement.

Current dependence. The frequency increases linearly with increasing current-density amplitude and it seems to be almost independent of the bias field for large current density. However, for J close to the critical current J_{c4}, the frequency drops almost vertically to zero since here the trajectory passes through the energy saddle point at which the frequency vanishes. This deviation is more strongly pronounced for larger bias field amplitudes for which $|J_{c4}|$ increases.

The linear increase of f vs J can be explained by considering that the frequencies of the OPP precessions are governed by the out-of-plane demagnetization field $4\pi M_s m_z$, which dominates over the anisotropy and bias field. Using expression Eq. (12b) for the average magnetization component $\langle m_z \rangle$, one can then estimate the (zero-bias field) preces-

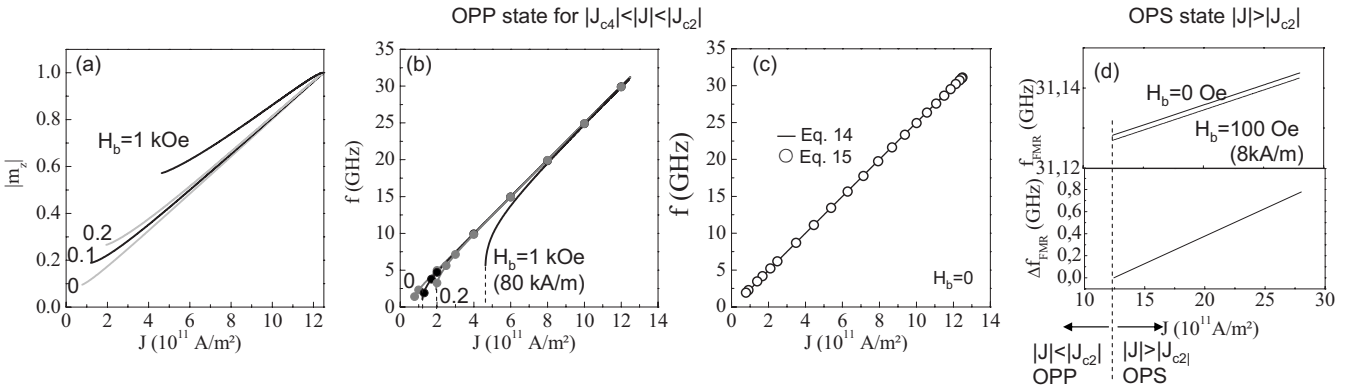

FIG. 7. (a)–(c) OPP steady-state precessions: (a) $|m_z|$ vs J and (b) f vs J for different bias fields H_b=0, 0.1, 0.2, and 1 kOe (0, 8, 16, and 80 kA/m): Full line according to Eq. (14) and dots from numerical integration of LLGS. (c) Comparison of the frequency calculated from Eqs. (14) and (15); (d) FMR frequency f_{FMR} and linewidth Δf_{FMR} for the OPS FMR-type precessions with $|J|>|J_{c2}|$ as discussed in Sec. VII.

sion frequency by Eq. (15) (Refs. 1, 35, and 36):

$$f = \frac{\gamma}{2\pi} 4\pi M_s \langle m_z \rangle,$$

$$f \approx \frac{\gamma}{2\pi} H_d \frac{a_j}{\alpha H_d} = \frac{\gamma}{2\pi} \left[\frac{\hbar}{2e} \frac{g(\eta)}{M_s t} \right] \frac{J}{\alpha}. \tag{15}$$

A comparison of this approximate evaluation with the numerical evaluation of Eq. (14) for H_b=0 is shown in Fig. 7(c), revealing good agreement.[35] Evidently though, this equation cannot reproduce the sharp drop of the frequency at the lower boundary J_{c4}.

From this approximate Eq. (15), the linear dependence of the precession frequency on the current density becomes evident. However, we also obtain a nonintuitive dependence of the precession frequency on the value of the saturation magnetization M_s. As can be seen, the frequency decreases upon increasing M_s, which would not be expected from the relation $f \sim 4\pi M_s m_z$. This dependence is due to the spin-polarization prefactor a_j that is inversely proportional to M_s.

Field dependence $f(H_b)$. In contrast to the linear increase in frequency f vs J the frequency decreases parabolically as a function of bias field amplitude H_b. This field dependence is shown in Fig. 8(a) for currents close to J_{c2} and in Fig. 8(b) for currents close to $J_{c1}(H_b=0)$ and $J_{c4}(H_b=0)$. Qualitatively the decrease in f with H_b can be understood by the fact that the in-plane bias field tilts the magnetization trajectory as shown in Fig. 6(c). Due to this tilt, the average component $\langle m_z \rangle$ decreases, thus decreasing f [see Eq. (15)]. It drops to zero when the critical boundary $J_{c4}(H_b)$ is crossed.

We like to note that this current and field dependence of the steady-state OPP oscillation frequencies is quite different from the current and field dependence of the in-plane (IPP) steady-state precessions induced by a planar polarizer[6,9,20,23,24,41] for which the frequency decreases as a function of current density and increases as a function of bias field. These opposite dependencies of IPP and OPP steady-state oscillations on J and H_b can thus be used to identify the mode character in experiments.[27]

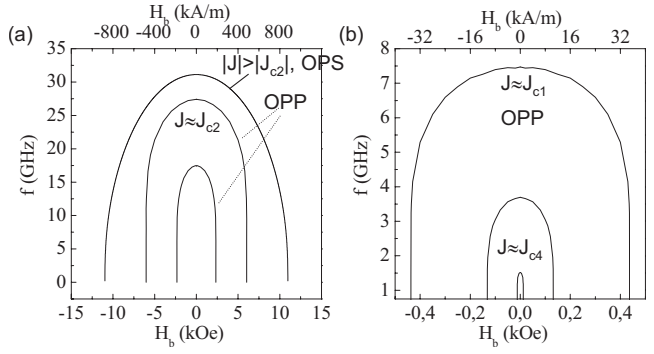

FIG. 8. Frequency vs bias field of OPP steady-state oscillations for different current-density amplitudes that are close to (a) J_{c2} and (b) the zero-bias field critical currents $J_{c1}(H_b=0)$ and $J_{c4}(H_b=0)$. In (a) the curve for $|J|>|J_{c2}|$ corresponds to the FMR-type oscillation around the static OPS state as discussed in Sec. VII.

D. Current interval of OPP oscillations

As given in Eqs. (10) and (11), as well as in Eq. (13), all three critical current densities J_{c1}, J_{c2}, and τ_x are proportional to the saturation magnetization M_s, the free layer thickness t, and the inverse of the spin-polarization efficiency $g(\eta)$. This dependence is due to the common spin torque prefactor a_j [Eq. (2)] and is the same for the planar polarizer. Thus a reduction in the critical current-density amplitudes J_{c1} and J_{c4} requires low M_s, a thin free layer, and a high spin polarization as for the planar polarizer.

This common prefactor is multiplied by a second term that reflects in the case of J_{c1} and J_{c2}, the type of instability described in Sec. III for which $\omega''=0$. For the OPS state, this second term is given by the linewidth term of Eq. (4) and therefore J_{c2} is proportional to the damping constant α and the demagnetization field [see Eq. (11)]. This is very similar to the critical current density of the planar polarizer for the transition from the IPS to the steady IPP state and results from the same type of instability [case (3a) of Sec. II].[41,42]

In contrast, the critical current density J_{c1}, Eq. (10) for the perpendicular polarizer is governed by the uniaxial anisotropy field H_u and the bias field H_b but is independent of α. From this, it follows that it should be possible to tune J_{c1} via

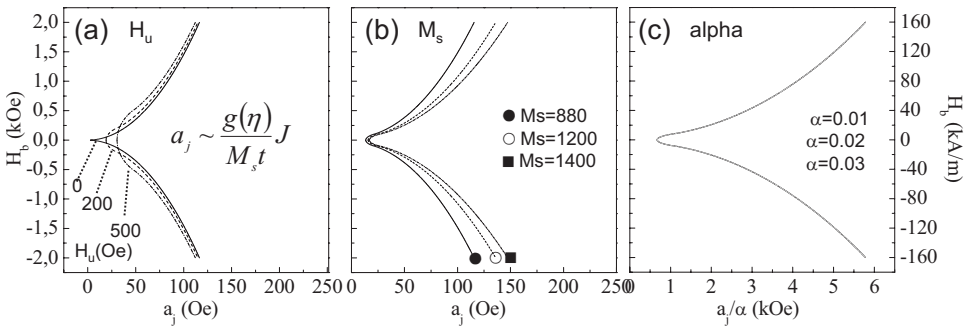

FIG. 9. Lower critical boundary $J_{c4}(H_b)$ plotted as a function of the scaled current $a_j \sim Jg(\eta,\theta_p)/M_s t$ for (a) different values of H_u: 0, 200, and 500 Oe (0, 16, and 40 kA/m) and (b) different values of M_s (in emu/cm^3 or kA/m) as indicated on the figure. (c) Expression Int_{c4} of Eq. (13b) plotted as a function of the scaled current $\mathbf{H}_{\mathrm{eff}}$ for different values of α. All curves are superposed.

the uniaxial anisotropy field H_u and, in particular, it should be possible to reduce J_{c1} to zero when $H_b=0$ and $H_u=0$.[35,36]

However, in order to determine the full current interval of OPP oscillations, the lower boundary J_{c4} is more relevant than J_{c1}. In this case the common prefactor is multiplied by a term noted as $\alpha \mathrm{Int}_{c4}$ in Eq. (13b). Its dependence on H_u and M_s is shown in Fig. 9 for the scaled current a_j. As for J_{c1}, the boundary J_{c4} can be tuned by the anisotropy field [see Fig. 9(a)], in particular around $H_b=0$ where J_{c4} goes to zero for $H_u=0$. For larger bias field values, however, the influence of the anisotropy field is less important. Furthermore, the scaled boundary J_{c4} is only weakly dependent on M_s [see Fig. 9(b)]. Finally there is no additional dependence on the damping constant $a_j=0$ in the expression Int_{c4} of Eq. (13b) as shown in Fig. 9(c), where Int_{c4} is plotted as a function of the scaled current a_j/α.

We like to note that although the dependencies of J_{c1} and J_{c4} on α, H_u, and M_s are somewhat different they both describe the transition between the IPS and OPP state for increasing and decreasing current-density amplitude, respectively. They are, therefore, both characterized by a jump of the magnetization component m_z between the IPS state ($m_z=0$) and the OPP state ($m_z \neq 0$) [see Fig. 6(d)].

Since both the lower boundary J_{c4} and the upper boundary J_{c2} of OPP oscillations depend on the damping parameter, α can be included into the common prefactor $\alpha M_s t/g(\eta)$, which represents a scaling of the current axis. This means that the current-density interval of steady-state OPP oscillations $[J_{c4},J_{c2}]$ can be tuned by varying α, $g(\eta)$, or the free layer thickness t while keeping the frequency range constant. This becomes more evident upon replacing in the expression for the frequency [Eq. (15)], the corresponding critical current densities J_{c2} [Eq. (11)] and J_{c4} [Eq. (13)] for J. This yields an estimate for the upper and lower bounds of the precession frequency that are independent of the current interval and are given by the materials parameters [Eq. (16)]:

$$\frac{\gamma}{2\pi} \times \mathrm{Int}_{c4} < f < \frac{\gamma}{2\pi}\left(H_d + \frac{H_u}{2}\right). \tag{16}$$

In Eq. (16), the common prefactor $\alpha M_s t/g(\eta,q_p)$ disappears since the frequency and the critical current depend in an inverse manner on this factor. The full frequency range of OPP oscillations is thus in fact independent of this factor and is only given by the demagnetization field (upper bound) and the expression Int_{c4} of Eq. (13) (lower bound), which depends on H_b, H_u, and weakly on M_s [see Fig. 9]. This scaling is illustrated in Fig. 10(a) where it can be seen that the lower and upper bounds of the frequency remain unchanged upon changing, for example, the damping constant α from 0.01 to 0.02, while the current-density interval doubles. Varying, however, M_s will not only scale the current axis but will also increase the upper frequency bound [Eq. (16)] as is illustrated in Fig. 10(b) for three values of M_s. From this, the inverse dependence of the frequency on M_s becomes also evident. As mentioned above, at a given value of J, the frequency decreases for increasing M_s.

E. Angular dependence of $g(\eta,\theta_p)$

The scaling of the current axis with the spin-polarization efficiency factor discussed in the previous section is an indirect justification for using a constant value of $g(\eta,\theta_p=90°)$

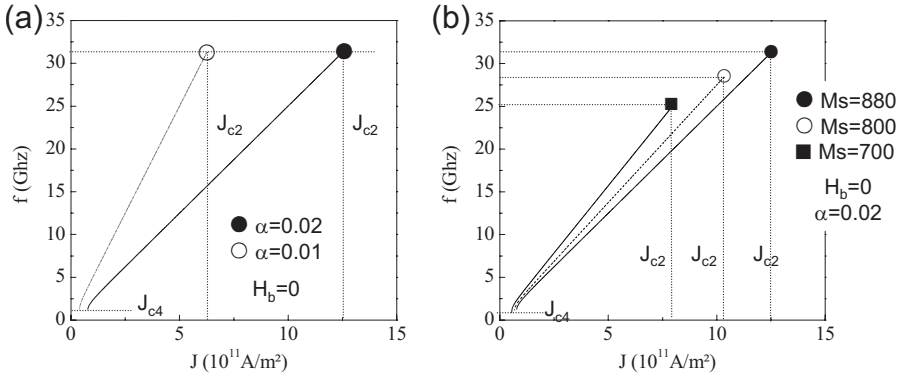

FIG. 10. Frequency vs current density for (a) two different values of the damping constant α and (b) three different values of M_s (in emu/cm^3 or kA/m).

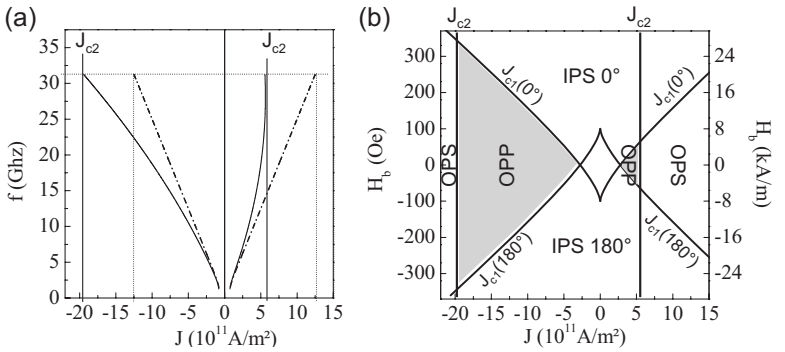

FIG. 11. (a) Comparison of the frequency vs current density for a constant spin-polarization efficiency $g(\eta)$ (dash-dotted line) and for an angular dependent $g(\eta,\theta_p)$ (full line). (b) State diagram showing J_{c1} and J_{c2} for an angular dependent $g(\eta,\theta_p)$ using the parameters of Table I.

$=g(\eta)=$const in order to extract the essential properties of the perpendicular polarizer configuration. A constant $g(\eta)$ results in a symmetric dependence of the critical lines as well as of the frequency vs J, which therefore have been given in most figures for only one current direction. However, taking the angular dependence of $g(\eta,\theta_p)$ into account will lead to some important asymmetries with respect to the sign of the current, which should be measurable in the experiment and which need therefore to be mentioned here. The spin-polarization efficiency varies as a function of the relative angle θ_p between **M** and **P**. For "conventional" ("nonwavy"[25]) spin valve structures, the dependence of $g(\eta,\theta_p)$ (Refs. 1, 7, and 41) is such that the spin torque amplitude is much weaker close to the parallel configuration ($\theta_p=0°$) than close to the antiparallel configuration ($\theta_p=180°$). Therefore, for the perpendicular polarizer for which the zero-current orientation is $\theta_p=90°$, the spin torque increases for positive current density since here **M** rotates antiparallel to **P**, while for negative current density the spin torque decreases since **M** rotates parallel to **P**. Consequently, taking the angular dependence of $g(\eta,\theta_p)$ into account results in a "local scaling" of the current axis for each current value. This nonconstant scaling leads to a nonlinear increase in f vs J, as shown in Fig. 11(a) where the frequency-current dispersion for a constant (dashed line) spin-polarization efficiency factor is compared to an angular dependent (full line) one. The angular dependence does not change the upper frequency limit but reduces the current-density interval for positive current density while it increases the current-density interval for negative current density. This leads to a positive curvature of f vs J for $J>0$ and a negative curvature for $J>0$.

This asymmetry is also reflected in the state diagram. While J_{c1} and J_{c4} are not (or very little) affected,[50] the value of the boundary J_{c2} decreases (increases) for $J>0$ ($J<0$) as illustrated in Fig. 11(b) (only J_{c1} and J_{c2} are shown for clarity).

V. COMPARISON TO EXPERIMENT

In this section, we will compare the macrospin simulation with recent experiments that have been performed for a "perpendicular polarizer–planar free layer–planar analyzer" spin valve structure.[27] For the current range that has been investigated, the experimental critical current density J_c^{expt} is very similar to the critical current density J_{c1} shown in Fig. 3(a), bounding a triangular shaped region of OPP steady-state oscillations in the current-field plane. The experimental results $J_c^{\mathrm{expt}}(H_b)$ are plotted in Fig. 12(a) (dots) in comparison to the calculated $T=0$ K state diagram [full lines for $J_{c1}(H_b)$ and $J_{c4}(H_b)$], using the parameters of Table I. A number of differences can be noted: (i) in the experiments the values of the critical current density J_c^{expt} and the associated slopes $dJ_c^{\mathrm{expt}}/dH_b$ are lower than those for J_{c1} but larger than those for J_{c4}; (ii) the inner bistable IPS 0°/IPS 180° region of Fig. 3(a) is absent in the experiment.

In Fig. 12(b) we also compare the experimental frequencies with those calculated for the full range of OPP oscillations starting at J_{c4}. In the experiments two frequency branches exist, a low current branch called $f1$ and a high current branch called $f2$. As discussed in Ref. 50, the magnetization on branch $f1$ is supposed to be macrospinlike while the magnetization of branch $f2$ adopts a nonuniform micromagnetic configuration. Thus only branch $f1$ can be considered here. While the onset of the frequencies of branch $f1$ seems to coincide with macrospin simulations, the slope df/dJ is lower in the experiment leading to overall lower values of the frequencies. Furthermore, the asymmetry of df/dJ with respect to the current direction appears to be different than the one indicated in Fig. 11(a).

Since the values for both the critical current density and the frequency are lower in the experiment than the critical current density J_{c1} and f in the simulation, and because their dependence on the common factor $M_s t/g(\eta,\theta_p)$ is inverse [compare to Eqs. (10), (13), and (15)], it is not possible to adjust, for example, the spin polarization η to fit both sets of data simultaneously. Therefore, further parameters must play a role.

Besides these differences for the critical currents and the frequencies, we also note that in the experimental magnetoresistance (MR)-bias field transfer curves [Fig. 12(c)] there is only a very small hysteresis for the transition from the OPP state [plateau of the MR curves Fig. 12(c)] to the IPS-P (parallel) or IPS-AP (antiparallel) state. However, from the $T=0$ K simulations a relatively large hysteresis is expected, as shown in Fig. 12(d) (dashed lines), due to the IPS/OPP bistability region bounded by J_{c1} and J_{c4} (see Fig. 5).

From this last observation we conclude that thermal activation plays an important role for the free layer dynamics under spin torque. We therefore have performed macrospin simulations to calculate the hysteresis loop including a thermal noise field corresponding to a given effective temperature T_{eff} (Ref. 51) (see Appendix D). From these simulations

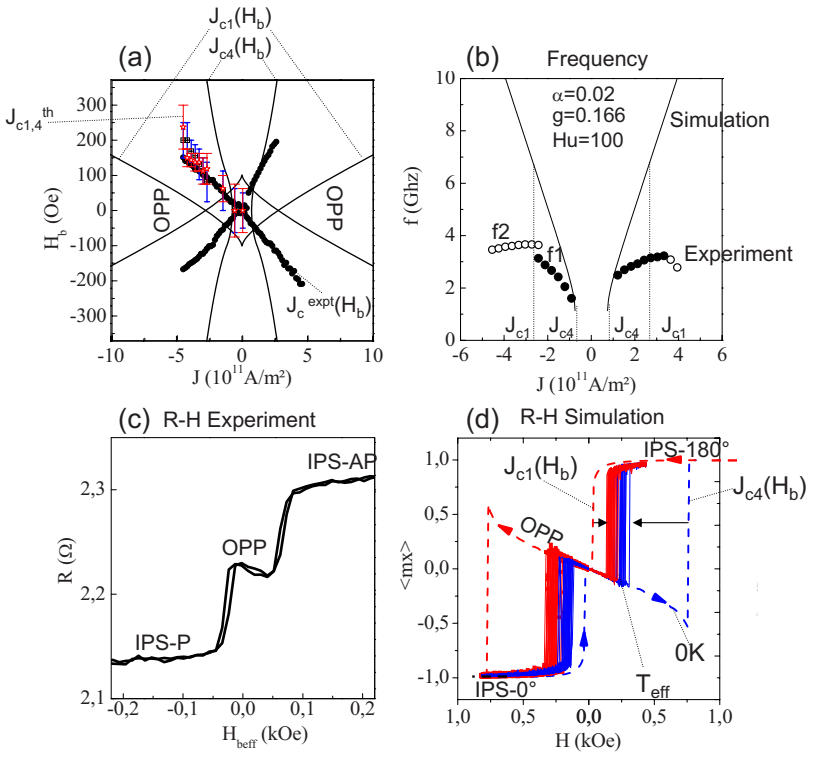

FIG. 12. (Color online) Comparison between experiments (Ref. 27) and macrospin simulations. (a) Experimental critical current density J_c^{expt} bounding OPP oscillations (black dots), calculated $T=0$ K boundaries J_{c1} and J_{c4} (full black lines), and calculated $T_{eff}=2000$ K boundaries J_{c1}^{th} (red dots) and J_{c4}^{th} (blue dots). (b) Experimental frequency vs current density J: branch $f1$ (full dots) and branch $f2$ (open dots), and simulated $T=0$ K frequency (full line). (c) Experimental resistance R vs effective bias field $H_{b\,eff}$ hysteresis. Here IPS-P and IPS-AP correspond to the static IPS 0° and IPS 180° states, respectively. (d) Simulated hysteresis (in terms of $\langle m_x \rangle$) for $T=0$ K (red and blue dashed lines) and $T_{eff}=2000$ K (red and blue full lines).

we observe that the boundaries J_{c1} and J_{c4} move toward each other upon increasing T_{eff}, with J_{c4} being much more sensitive. At sufficiently high T_{eff} both lines seem to coincide within the error bars, that are given by the limited number (20) of realizations performed. For comparison, hysteresis loops at $T_{eff}=2000$ K are shown in Fig. 12(d), where it is evident that the hysteresis between the OPP and IPS states has vanished. The large value of the effective temperature T_{eff} should not be taken too literally and is explained by the different scan rates of the bias field used in the simulations (80 Oe/50 ns) and in the experiments (10 Oe/s). In the case of the simulation this scan rate is too fast for thermal effects at room temperature to be noticeable. This has therefore been compensated for by artificially increasing the temperature.[41]

The calculated thermal boundaries J_{c1} and J_{c4} are superposed in Fig. 12(a) ($J_{c1,4}^{th}$) and they seem to be quite close to the experimental data J_c^{expt}. This suggests that thermal activation reduces the hysteresis between J_{c1} and J_{c4}, explaining the apparent decrease in J_c^{expt} and the slope dJ_c^{expt}/dH_b as compared to J_{c1}. In contrast, the reduced values of the frequencies cannot be explained satisfactorily by macrospin simulations and neither can the asymmetry of the slopes df/dJ by varying the parameters α and $g(\eta,\theta_p)$ in a reasonable range of parameters.

VI. SMALL ANGLE DAMPED EXCITATIONS AROUND THE STATIC IPS AND OPS STATES

In order to complete the theoretical macrospin description for the perpendicular polarizer-planar free layer configuration, we will describe in this section the small amplitude damped excitations around the static IPS and OPS states.

These damped excitations should not be confused with the steady-state OPP oscillations described in Sec. IV, which are nonlinear (large amplitude) and which correspond to unstable solutions of the LLGS Eq. (2) {the imaginary part of the complex frequency [Eq. (4)] being positive, $\omega''>0$}.

In contrast to this, the damped oscillations correspond to linear (small amplitude) excitations around a well defined static stable state (θ_o,φ_o). These excitations can thus be considered as ferromagnetic resonance excitations in the presence of spin torque and can be studied experimentally, for example, by perturbing the system using a small rf pumping field or an ac current[32,34] or by measuring the thermal noise spectra.[33]

The conditions for the observation of the linear damped oscillations are thus:

(i) the existence of a static stable state that corresponds to $\omega''<0$ (Sec. II), where ω'' provides the frequency linewidth of the excitations;

(ii) a nonzero real part $\omega'\neq 0$ that provides the precession frequency of the excitations, which in the following we call FMR frequency in order to better distinguish them from the frequencies of steady-state oscillations discussed in Sec. IV.

A. Damped oscillations around the IPS state for $|J|<|J_{c1}|$

First we will address the excitations around the static IPS states defined by Eq. (8) for current-density amplitudes that are smaller than the critical current J_{c1}, $|J|<|J_{c1}|$ [in the approximation of a constant spin-polarization factor $g(\eta)$ =const]. Evaluating the complex frequency Eq. (4) for the static positions [Eq. (8)], we obtain the precession frequency of the excitations [Eq. (17a)] from the square-root term (real part ω') and the linewidth [Eq. (17b)] from the linewidth term (imaginary part ω''):

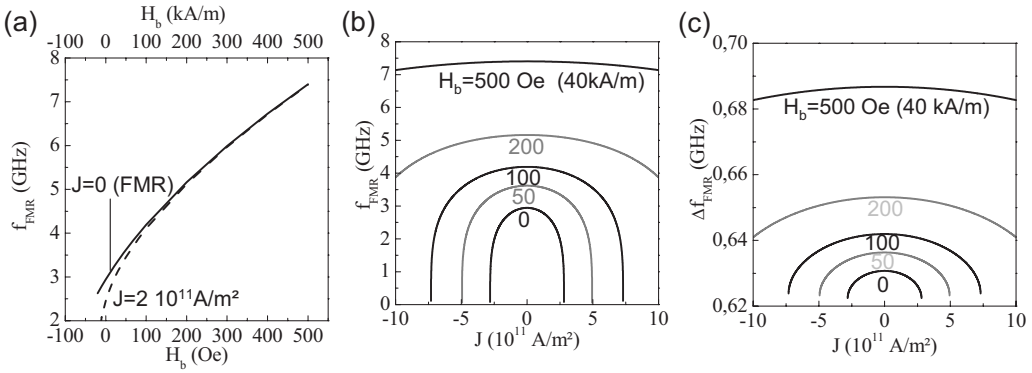

FIG. 13. (a) FMR frequency vs bias field H_b for the IPS 0° state for $J=0$ (black line) and $J=2\times10^{11}$ A/m$^2<J_{c1}(H_b=0)$ (dashed line). The frequencies of the IPS 180° state would be similar but with the field axis inverted. (b) FMR frequency vs current density J and (c) FMR linewidth vs J. In (b) and (c) the numbers give the respective field values of H_b in Oe (kA/m).

$$\frac{\omega'}{\gamma'} = -\sqrt{(1+\alpha^2)(H_u\ \cos\ 2\varphi_o + H_b\ \cos\ \varphi_o)(H_u \cos^2\varphi_o + H_b\ \cos\ \varphi_o + H_d) - \left(\frac{\omega''}{\gamma'}\right)^2},$$

$$\frac{\omega'}{\gamma'} \approx \sqrt{(H_u\ \cos 2\varphi_o + H_b \cos\varphi_o)(H_u \cos^2\varphi_o + H_b \cos\varphi_o + H_d)}, \tag{17a}$$

$$\frac{\omega''}{\gamma'} = -0.5\alpha(H_u \cos^2\varphi_o + H_u \cos 2\varphi_o + 2H_b \cos\varphi_o + H_d). \tag{17b}$$

Numerical evaluation of Eq. (17) is plotted in Fig. 13 showing the FMR frequency f_{FMR} and the corresponding linewidth Δf_{FMR} for the IPS 0° state as a function of current and bias field.

The increase in f_{FMR} with H_b in the presence of a spin polarized current is very similar to the zero-current FMR frequencies [see Fig. 13(a)]. In particular, for large bias field amplitudes the frequencies are very close since at a constant current-density amplitude the in-plane rotation φ_o decreases with increasing bias field amplitude [see Fig. 3(b)]. In contrast, at low and reverse fields where the magnetization is antiparallel to the bias field, the frequencies deviate strongly. In particular, the frequencies drop to zero at smaller (reverse) field values, which is due to the reduction in the coercive field with increasing current-density amplitude for the bistable IPS 0°/IPS 180° region shown in Fig. 3(a) (gray shaded area). This deviation becomes more evident when looking at the current-density dependence shown in Fig. 13(b). Here the frequency decreases in a parabolic way upon increasing the current density in both positive and negative directions.

It is of interest to compare the frequency-current dispersion f_{FMR}-J in the subthreshold regime ($|J|<|J_{c1}|$) for the perpendicular polarizer with the one for the planar polarizer (with $\mathbf{H}_u$, $\mathbf{H}_b$, and $\mathbf{P}$ being collinear). The latter has been recently studied experimentally for magnetic tunnel junctions[33] and has shown a relatively weak variation of the FMR frequency vs J, while in the macrospin approach the corresponding linewidth is supposed to go to zero at the critical current density. In contrast, for the perpendicular polarizer case a much more pronounced dependence of the FMR frequency vs current density is expected from Fig. 13(b) while the linewidth varies little (few tens of MHz). In particular, the frequency drops to zero close to the critical current density J_{c1}.

This difference between the planar and perpendicular polarizer is due to the following: In the planar polarizer case, the static position φ_o is independent of the current ($\varphi_o \| \text{energy minimum}$), and the frequency [square-root term of Eq. (4)] contains direct contributions from the spin torque which are proportional to a_j (with $P_r' \neq 0$). These terms, however, are small as compared to the dominating ω_o term in the square root, leading to an overall weak dependence of the FMR frequency on the current density.

In contrast, for the perpendicular polarizer case, the polarization component P_r' is zero [see Eq. (4) for $\theta_o=90°$ and $\mathbf{P}=(0,0,1)$] so that the direct contributions from the a_j terms vanish in the square-root expression, Eq. (4). The current dependence is indirectly given via the current dependence of the equilibrium angle φ_o, which enters the ω_o and $\Delta\omega$ terms in Eq. (4). Since φ_o varies strongly with current and bias field [see Fig. 3(b)], this provides a much stronger dependence of the resonance frequency on the current density, in particular at low bias field. Furthermore, the FMR frequencies and linewidths are symmetric with respect to the sign of the current [see Figs. 13(b) and 13(c)], yielding the same shift in FMR frequency and the same decrease in the linewidth with increasing amplitude of J. This symmetry expresses the fact that, for the perpendicular polarizer in the subthreshold regime ($|J|<|J_{c1}|$), the spin polarized current is not acting as an enhanced damping (stabilization) for one

current direction or as "antidamping" (destabilization) for the other current direction. The major effect of the current in the subthreshold regime is a rotation of the static equilibrium state. This is quite different from the planar polarizer case or the FMR oscillations around the OPS state where the current can enhance or decrease the effective damping.[33,52,53]

B. Damped oscillations around the OPS state

The FMR frequency and linewidth [Eq. (18)] for the oscillations around the stable OPS state are obtained in analogy to the IPS state upon inserting the (approximate) static states Eq. (9b) into the complex frequency Eq. (4):

$$\frac{\omega'}{\gamma'} = \sqrt{H_d\left[\frac{(H_u+H_d)^2-H_b^2}{(H_u+H_d)}\right] - \alpha|a_j|\frac{\sqrt{(H_u+H_d)^2-H_b^2}[H_b^2-(H_u+H_d)(H_u+2H_d)]}{(H_u+H_d)^2}},$$

$$\frac{\omega'}{\gamma'} \approx \sqrt{(H_d^2-H_b^2) - \alpha|a_j|\frac{\sqrt{H_d^2-H_b^2}[H_b^2-2H_d^2]}{H_d^2}} \approx \sqrt{(H_d^2-H_b^2)}, \tag{18a}$$

$$\frac{\omega''}{\gamma} = \frac{1}{2}\left[\alpha\frac{(H_u+H_d)(H_u+2H_d)-H_b^2}{(H_u+H_d)} - 2|a_j|\frac{\sqrt{(H_u+H_d)^2-H_b^2}}{(H_u+H_d)}\right],$$

$$\frac{\omega''}{\gamma} \approx \frac{1}{2}\left[\alpha\left(\frac{2H_d^2-H_b^2}{H_d}\right) - 2|a_j|\frac{\sqrt{H_d^2-H_b^2}}{H_d}\right]. \tag{18b}$$

Numerical evaluation of Eq. (18) is shown in Fig. 7(d) for the current dependence and in Fig. 8(a) for the field dependence (top curve). As can be seen, the field dependence shows a parabolic behavior similar to the OPP oscillations. This parabolic dependence is more evident when neglecting, in Eq. (18a), H_u and α, as has also been derived in Ref. 8.

In contrast to the strong field dependence, the corresponding dependence of the FMR frequency on the current density is quite weak [see Fig. 7(c)]. However, the linewidth varies strongly and goes to zero at J_{c2}. This is in contrast to the IPS case, Fig. 13(c), but is very similar to the behavior of a planar polarizer at the transition from the static stable state to the in-plane precession state[6,11,41,42,52,53] due to the same type of instability [condition (3a) of Sec. II].

VII. SUMMARY

For the "perpendicular polarizer-planar free layer," the state diagram in the current-field plane has been derived from linear stability analysis in a zero-temperature macrospin approach. Three different states exist, which are the in-plane stable (IPS) state, the out-of-plane stable state (OPS), and the steady-state out-of-plane precession (OPP). No steady-state IPPs are observed. The boundaries between the different static and dynamic states have been obtained and different regions of bistability have been identified. In particular, there is a large hysteresis for increasing and decreasing current and bias field between the IPS and the OPP state, which is much reduced or disappears when thermal fluctuations are taken into account. In comparison to the more commonly known "planar polarizer-planar free layer" oscillator, the state diagram for the perpendicular polarizer configuration is symmetric in the current and bias field plane with oscillations that occur in zero applied bias field, which is of importance for device realization. Furthermore, the nature of the transition from the static IPS state to the steady-state oscillation state is quite different for the planar and perpendicular polarizer, the transition of the latter being characterized by an abrupt jump of the out-of-plane magnetization component m_z and the frequencies.

For the OPP steady-state oscillations, the frequency dispersion vs current and bias field has been determined revealing a linear increase in f vs J[35] and a parabolic decrease in f vs H_b. This dependence is quite different from IPP oscillations induced by a planar polarizer where the frequency decreases with current and increases with bias field. The upper and lower bound of the frequency of the steady-state OPP oscillations induced by the perpendicular polarizer is independent of the spin-polarization efficiency $g(\eta,\theta_p)$ and the damping constant α, but it depends weakly on the bias field and anisotropy (lower bound) as well as on the saturation magnetization M_s (upper bound). The corresponding current interval where these oscillations occur can be scaled by the saturation magnetization M_s, the free layer thickness t, $g(\eta,\theta_p)$, and α.

We also deduced the FMR frequency for small amplitude oscillations around the static IPS and OPS state that are obtained when a small perturbation is applied to the static state. For the IPS state, the spin polarized current does not contribute to the effective damping of these FMR excitations and the dependence of the FMR frequency on current is given indirectly from the rotation of the magnetization away from its zero-current energy minimum.

ACKNOWLEDGMENTS

This work was supported in part by the French national program ANVAR Grant No. A0503013 and the French National Research Agency (ANR) through the programs CARNOT and PNANO (MagICO Grant No. ANR-05-NANO-

044), as well as partially by the EC program DYNAMICS Grant No. HPRN-CT-2002-00289. I.F. acknowledges support from the CARNOT program. We thank A. Slavin, V. Tiberkevich, and C. Baraduc for the very stimulating discussions.

APPENDIX A: ROTATION MATRIX

For the transformation of a vector $\boldsymbol{A}$ in Cartesian coordinates to the vector $A' = \underline{\underline{R}} A$ in the local spherical coordinates, we have used the following rotation matrix [Eq. (A1)]:

$$\underline{\underline{R}} = \begin{pmatrix} \sin\theta_o \cos\varphi_o & \sin\theta_o \sin\varphi_o & \cos\theta_o \\ \cos\theta_o \cos\varphi_o & \cos\theta_o \sin\varphi_o & -\sin\theta_o \\ -\sin\varphi_o & \cos\varphi_o & 0 \end{pmatrix}, \quad \text{(A1)}$$

where (θ_o, φ_o) are the coordinates of the static position.

APPENDIX B: LINEARIZATION

The linearization of the LLGS equation [Eq. (2)] in the local spherical coordinates has been performed by using the following development of the effective field $\mathbf{H}'_{\text{eff}}$ [Eqs. (B1)–(B3)] and the spin torque term [Eq. (B4)] in terms of the dynamic variable $\delta\mathbf{m}'$ around the static equilibrium magnetization $\mathbf{M}'_o$.

Development of the effective field:

$$\begin{aligned} \mathbf{H}'_{\text{eff}} &= \mathbf{H}'_{\text{eff}}(\mathbf{M}') \\ &= \mathbf{H}'_{\text{eff}}(\mathbf{M}'_o + \delta\mathbf{m}') \\ &= \mathbf{H}'_{\text{eff}}(\mathbf{M}'_o) + \left.\frac{\partial \mathbf{H}'_{\text{eff}}(\mathbf{M}')}{\partial \mathbf{M}'} \delta\mathbf{m}'\right|_{\mathbf{M}'_o} \\ &= \mathbf{H}'_{\text{eff}}(\mathbf{M}'_o)|_{\text{static}} + \mathbf{h}'_{\text{eff}}|_{\text{dynamic}}, \end{aligned} \quad \text{(B1)}$$

with

$$\mathbf{H}'_{\text{eff}}(\mathbf{M}'_o) = -\left.\frac{\partial E}{\partial \mathbf{M}'}\right|_{\mathbf{M}'_o} = -\left.\frac{1}{M_s}\frac{\partial E}{\partial \theta}\mathbf{e}_\theta - \frac{1}{M_s \sin\theta}\frac{\partial E}{\partial \varphi}\mathbf{e}_\phi\right|_{\mathbf{M}'_o} \quad \text{(B2)}$$

and

$$\begin{aligned} \mathbf{h}'_{\text{eff}}|_{\text{dynamic}} &= \left.\frac{\partial \mathbf{H}'_{\text{eff}}(\mathbf{M}')}{\partial \mathbf{M}'} \delta\mathbf{m}'\right|_{\mathbf{M}'_o} \\ &= \left.\left(\delta\mathbf{m}' \frac{\partial}{\partial \mathbf{M}'}\right)\mathbf{H}'_{\text{eff}}(\mathbf{M}')\right|_{\mathbf{M}'_o}, \end{aligned}$$

$$\begin{aligned} \mathbf{h}'_{\text{eff}}|_{\text{dynamic}} &= \left.\left(\delta m_\theta \frac{\partial}{M_s \partial\theta} + \delta m_\varphi \frac{1}{M_s \sin\theta}\frac{\partial}{\partial\varphi}\right)\mathbf{H}'_{\text{eff}}(\mathbf{M}')\right|_{\mathbf{M}'_o} \\ &= \left.\left(0, -\frac{1}{M_s^2} E_{\theta\theta}\delta m_\theta - \frac{1}{M_s^2 \sin\theta} E_{\theta\varphi}\delta m_\varphi, \right.\right. \\ &\quad \left.\left. -\frac{1}{M_s^2 \sin\theta} E_{\theta\varphi}\delta m_\theta - \frac{1}{M_s^2 \sin^2\theta} E_{\varphi\varphi}\delta m_\varphi\right)\right|_{\mathbf{M}'_o} \end{aligned} \quad \text{(B3)}$$

with

$$\delta m_\theta = M_s \delta\theta \text{ and } \delta m_\varphi = M_s \sin\theta \delta\varphi.$$

Development of the spin torque term (neglecting the angular dependence of the prefactor a_j):

$$\begin{aligned} \mathbf{M}' \times (\mathbf{M}' \times \mathbf{P}') &= (\mathbf{M}'_o + \delta\mathbf{m}') \times [(\mathbf{M}'_o + \delta\mathbf{m}') \times \mathbf{P}'] \\ &\approx (\mathbf{M}'_o) \times (\mathbf{M}'_o \times \mathbf{P}') + (\mathbf{M}'_o) \times (\delta\mathbf{m}' \\ &\quad \times \mathbf{P}') + (\delta\mathbf{m}') \times (\mathbf{M}'_o \times \mathbf{P}'). \end{aligned} \quad \text{(B4)}$$

APPENDIX C: COORDINATE SYSTEM

Depending on the stable point considered, one has to take care in choosing the correct Cartesian coordinate system due to the singularity at $\theta = 0°$. For the out-of-plane stable state, therefore, the thin film geometry is rotated with respect to the coordinate system shown in Fig. 1(b) such that the easy axis is along the z axis and the normal to the film plane along the x axis. Without noting, all equations related to the OPS state have been calculated in this way [Eqs. (9), (11), and (18)]. However, throughout the text all vectors are expressed in the geometry defined in Fig. 1(b) in order not to complicate the reading.

APPENDIX D: THERMAL MACROSPIN SIMULATIONS

Thermal fluctuations are accounted for by adding a random-fluctuating field $\mathbf{H}_{\text{fl}}$ to the effective field $\mathbf{H}_{\text{eff}}$ in the LLGS Eq. (2). This fluctuating field is a Gaussian random process verifying the statistical properties:[51]

$$\langle H_{\text{fl},i} \rangle = 0, \quad i = x, y, z,$$

$$\langle H_{\text{fl},i}(t) H_{\text{fl},j}(t') \rangle = 2D\delta_{ij}\delta(t - t'). \quad \text{(D1)}$$

Here $D = \frac{\alpha k_B T}{\gamma_0 \mu_0 M_s V}$ is the strength of the thermal fluctuations, where V is the volume of the sample, T is the temperature, M_s is the saturation magnetization value, and k_B is the Boltzmann constant.

[1] J. C. Slonczewski, J. Magn. Magn. Mater. **159**, L1 (1996); **195**, 261 (1999).
[2] L. Berger, Phys. Rev. B **54**, 9353 (1996).
[3] J. C. Slonczewski, U.S. Patent No. US5695864 (1997).
[4] Y. B. Bazaliy, B. A. Jones, and S. C. Zhang, Phys. Rev. B **57**, R3213 (1998).
[5] J. Z. Sun, Phys. Rev. B **62**, 570 (2000).
[6] Z. Li and S. Zhang, Phys. Rev. B **68**, 024404 (2003).
[7] J. Xiao, A. Zangwill, and M. D. Stiles, Phys. Rev. B **72**, 014446 (2005).

[8] A. N. Slavin and V. S. Tiberkevich, Phys. Rev. B **72**, 094428 (2005).
[9] A. N. Slavin and P. Kabos, IEEE Trans. Magn. **41**, 1264 (2005).
[10] S. M. Rezende, F. M. de Aguiar, and A. Azevedo, Phys. Rev. Lett. **94**, 037202 (2005); Phys. Rev. B **73**, 094402 (2006).
[11] G. Bertotti, C. Serpico, I. D. Mayergoyz, A. Magni, M. d'Aquino, and R. Bonin, Phys. Rev. Lett. **94**, 127206 (2005).
[12] K. J. Lee, A. Deac, O. Redon, J. P. Nozières, and B. Dieny, Nat. Mater. **3**, 877 (2004).
[13] J. Grollier, V. Cros, H. Jaffrès, A. Hamzic, J. M. George, G. Faini, J. B. Youssef, H. Le Gall, and A. Fert, Phys. Rev. B **67**, 174402 (2003).
[14] J. A. Katine, F. J. Albert, R. A. Buhrman, E. B. Myers, and D. C. Ralph, Phys. Rev. Lett. **84**, 3149 (2000).
[15] E. B. Myers, F. J. Albert, J. C. Sankey, E. Bonet, R. A. Buhrman, and D. C. Ralph, Phys. Rev. Lett. **89**, 196801 (2002).
[16] A. Deac, K. J. Lee, Y. Liu, O. Redon, M. Li, P. Wang, J. P. Nozières, and B. Dieny, Phys. Rev. B **73**, 064414 (2006).
[17] J. Hayakawa, S. Ikeda, Y. M. Lee, T. Meguro, F. Matsukura, H. Takahashi, and H. Ohno, Jpn. J. Appl. Phys., Part 2 **44**, L1267 (2005).
[18] W. Chen, M. J. Rooks, N. Ruiz, J. Z. Sun, and A. D. Kent, Phys. Rev. B **74**, 144408 (2006).
[19] A. V. Nazarov, H. M. Olson, H. Cho, K. Nikolaev, Z. Gao, S. Stokes, and B. B. Pant, Appl. Phys. Lett. **88**, 162504 (2006); A. V. Nazarov, K. Nikolaev, Z. Gao, H. Cho, and D. Song, J. Appl. Phys. **103**, 07A503 (2008).
[20] S. I. Kiselev, J. C. Sankey, I. N. Krivirotov, N. C. Emley, R. J. Schoelkopf, R. A. Buhrman, and D. C. Ralph, Nature (London) **425**, 380 (2003).
[21] S. I. Kiselev, J. C. Sankey, I. N. Krivorotov, N. C. Emley, M. Rinkoski, C. Perez, R. A. Buhrman, and D. C. Ralph, Phys. Rev. Lett. **93**, 036601 (2004).
[22] W. H. Rippard, M. R. Pufall, S. Kaka, T. J. Silva, and S. E. Russek, Phys. Rev. B **70**, 100406(R) (2004).
[23] W. H. Rippard, M. R. Pufall, S. Kaka, S. E. Russek, and T. J. Silva, Phys. Rev. Lett. **92**, 027201 (2004).
[24] Q. Mistral, J. V. Kim, T. Devolder, P. Crozat, C. Chappert, J. A. Katine, M. J. Carey, and K. Ito, Appl. Phys. Lett. **88**, 192507 (2006).
[25] O. Boulle, V. Cros, J. Crollier, L. G. Pereira, C. Deranlot, F. Petroff, G. Faini, J. Barnas, and A. Fert, Nat. Phys. **3**, 492 (2007).
[26] S. Mangin, D. Ravelosona, J. A. Katine, M. J. Carey, B. D. Terris, and E. E. Fullerton, Nat. Mater. **5**, 210 (2006).
[27] D. Houssameddine, U. Ebels, B. Delaët, B. Rodmacq, I. Firastrau, F. Ponthenier, M. Brunet, C. Thirion, J.-P. Michel, L. D. Buda-Prejbeanu, M.-C. Cyrille, O. Redon, and B. Dieny, Nat. Mater. **6**, 447 (2007).
[28] M. R. Pufall, W. H. Rippard, S. Kaka, T. J. Silva, and S. E. Russek, Appl. Phys. Lett. **86**, 082506 (2005).
[29] W. H. Rippard, M. R. Pufall, S. Kaka, T. J. Silva, S. E. Russek, and J. A. Katine, Phys. Rev. Lett. **95**, 067203 (2005).
[30] S. Kaka, M. R. Pufall, W. H. Rippard, T. J. Silva, S. E. Russek, and J. A. Katine, Nature (London) **437**, 389 (2005).
[31] F. B. Mancoff, N. D. Rizzo, B. N. Engel, and S. Tehrani, Nature (London) **437**, 393 (2005).
[32] A. A. Tulapurkar, Y. Suzuki, A. Fukushima, H. Kubota, H. Maehara, K. Tsunekawa, D. D. Djayaprawira, N. Watanabe, and S. Yuasa, Nature (London) **438**, 339 (2005).
[33] S. Petit, C. Baraduc, C. Thirion, U. Ebels, Y. Liu, M. Li, P. Wang, and B. Dieny, Phys. Rev. Lett. **98**, 077203 (2007).
[34] J. C. Sankey, P. M. Braganca, A. G. F. Garcia, I. N. Krivorotov, R. A. Buhrman, and D. C. Ralph, Phys. Rev. Lett. **96**, 227601 (2006).
[35] K. J. Lee, O. Redon, and B. Dieny, Appl. Phys. Lett. **86**, 022505 (2005); O. Redon, B. Dieny, and B. Rodmacq, U.S. Patent No. US6,532,164 B2 (2003).
[36] A. D. Kent, B. Özyilmaz, and E. del Barco, Appl. Phys. Lett. **84**, 3897 (2004).
[37] H. Morise and S. Nakamura, Phys. Rev. B **71**, 014439 (2005).
[38] W. Jin, Y. Liu, and H. Chen, IEEE Trans. Magn. **42**, 2682 (2006).
[39] X. Zhu and J.-G. Zhu, IEEE Trans. Magn. **42**, 2670 (2006).
[40] I. Firastrau, U. Ebels, L. D. Buda-Prejbeanu, J. C. Toussaint, C. Thirion, and B. Dieny, J. Magn. Magn. Mater. **310**, 2029 (2007).
[41] M. D. Stiles and J. Miltat, in *Spin Dynamics in Confined Magnetic Structures III*, edited by B. Hillebrands and A. Thiaville (Springer, New York, 2006).
[42] T. Valet (unpublished), presentation F27 of the 5th International Symposium on Metallic Multilayers (MML '04), Boulder, CO, 7–11 June 2004.
[43] J. V. Kim, Phys. Rev. B **73**, 174412 (2006); J. V. Kim, V. Tiberkevich, and A. N. Slavin, Phys. Rev. Lett. **100**, 017207 (2008).
[44] N. Smith, J. A. Katine, J. R. Childress, and M. J. Carey, IEEE Trans. Magn. **41**, 2935 (2005).
[45] D. Polder and J. Smit, Rev. Mod. Phys. **25**, 89 (1953); J. Smit and H. G. Beljers, Philips Res. Rep. **10**, 113 (1955).
[46] L. Baselgia, M. Warden, F. Waldner, S. L. Hutton, J. E. Drumheller, Y. Q. He, P. E. Wigen, and M. Marysko, Phys. Rev. B **38**, 2237 (1988).
[47] M. Farle, Rep. Prog. Phys. **61**, 755 (1998), and references therein.
[48] I. Theodonis, N. Kioussis, A. Kalitsov, M. Chshiev, and W. Butler, Phys. Rev. Lett. **97**, 237205 (2006).
[49] D. Gusakova, I. Firastrau, A. Vedayev, D. Houssameddine, U. Ebels, J.-Ch. Toussaint, B. Dieny, and L. Buda-Prejbeanu, presentation SC15 of the 1st International Symposium on Advanced Magnetic Materials (ISAMMA2007), Jeju, Korea, 28 May–1 June 2007.
[50] I. Firastrau, D. Gusakova, D. Houssameddine, U. Ebels, M.-C. Cyrille, B. Delaet, B. Dieny, O. Redon, J.-Ch. Toussaint, and L. D. Buda-Prejbeanu, following paper, Phys. Rev. B **78**, 024437 (2008).
[51] W. F. Brown, Phys. Rev. **130**, 1677 (1963).
[52] I. N. Krivorotov, N. C. Emley, J. C. Sankey, S. I. Kiselev, D. C. Ralph, and R. A. Buhrman, Science **307**, 228 (2005).
[53] J. V. Kim, Q. Mistral, C. Chappert, V. S. Tiberkevich, and A. N. Slavin, Phys. Rev. Lett. **100**, 167201 (2008).